A Hand-held Laser Scanner based on Multi-camera Stereo-matching

Christoph Bender[1], Klaus Denker[1], Markus Friedrich[1], Kai Hirt[1], and Georg Umlauf[1]

1 **HTWG Konstanz, Computer Graphics Lab**
Brauneggerstr. 55, D-78462 Konstanz, Germany
chbender|kdenker|kahirt|mafriedr|umlauf@htwg-konstanz.de

Abstract

Most laser scanners in engineering are extended versions of tactile measuring machines. These high precision devices are typically very expensive and hardware modifications are not possible without impairing the precision of the device.

For these reasons we built our own laser-scanner system. It is based on a multi-camera reconstruction system developed for fast 3D face reconstructions. Based on this camera system, we developed a laser-scanner using GPU accelerated stereo-matching techniques and a hand-held line-laser probe. The resulting reconstruction is solely based on the known camera positions and parameters. Thus, it is not necessary to track the position and movement of the line-laser probe. This yields an inexpensive laser-scanner system where every hardware component can be modified individually for experiments and future extensions of the system.

1998 ACM Subject Classification I.3 Computer Graphics, I.3.1 Hardware Architecture, Input Devices, I.4 Image Processing and Computer Vision, I.4.8 Scene Analysis, Stereo

Keywords and phrases Laser scanner, 3D point clouds, stereo-matching, multi-camera

Digital Object Identifier 10.4230/OASIcs.VLUDS.2011.123

1 Introduction

There are two main principles used for laser measurements [11]: time-of-flight and triangulation scanners. Time-of-flight (TOF) scanners measure the time a laser pulse needs from the emitter to the scene and back to the camera. Because they allow a large measuring distance, they are used for airborne 3D scanning in geo-sciences as in [16] and for range sensing in robotics as in [10]. Thus, for hand-held scanning at low distances this technique is not applicable.

Triangulation scanners measure the displacements of a laser line as seen from one or more cameras placed in a known distance to the laser emitter. They usually provide a much better precision than TOF scanners, but can only be used at short distances. In engineering, they are used for reverse engineering and quality measurements [15]. This type of scanners are used for example for hand-held triangulation scanners for real-time meshing as given in [3]. This algorithm simplifies the use of triangulation scanners mounted on measurement arms, which are usually very expensive.

Therefore, we describe in this paper how to build a low cost laser scanner based on the multi-camera 3D-reconstruction system we presented in [4] and a hand-held line-laser probe. This enables us to experiment and modify every individual step and component of the method at low costs and without impairing the complete system.

Proceedings of IRTG 1131 - Visualization of Large and Unstructured Data Sets Workshop 2011.
Editors: Christoph Garth, Ariane Middel, Hans Hagen; pp. 123–133

OpenAccess Series in Informatics
Schloss Dagstuhl – Leibniz-Zentrum für Informatik, Dagstuhl Publishing, Germany


To this end, we first discuss related work and necessary prerequisites in Sections 2 and 3 before we describe the individual steps of our method: calibration (Section 4), line extraction (Section 5) and depth estimation (Section 6). We close with some results of our method and give a brief outlook to our further plans in Sections 7 and 8.

2 Related Work

Since TOF scanners require high-precision time measurements [11] these devices are usually expensive. Thus, for low cost scanning devices triangulation scanners are the most appropriate technology. A low cost laser scanner is described in [17]. Here, a web-cam and a line-laser probe is used. Because neither the laser position nor the intrinsic camera parameters are known, a known background pattern is used for camera calibration. The 3D coordinates of the laser line are approximated based on the plane of the line-laser probe's light fan.

While laser scanning techniques reconstruct only a single laser point or line at a time, e.g. [15], it might be faster and cheaper to use no lasers at all and reconstruct larger regions at a time. Structured light methods project a set of light pattern onto the scene. Similar to triangulation laser scanners they reconstruct the 3D information from the displacement of these light patterns for known camera positions [13, 7, 19]. Because of the light projection, these methods require a dark environment minimizing interfering light sources.

It is also possible to generate depth information without a light source. Stereo matching approaches like [8, 12, 14, 18, 4] use two or more cameras with known positions. They detect similar image regions in multiple images and use the camera positions to triangulate the depth information. However, stereo-matching is a low precision reconstruction method. It is prone to systematical errors from light conditions, reflections, and repetitions in the images.

Our laser scanning system uses traditional triangulation scanner techniques as in [11] as well as low cost scanner techniques, see e.g. [17]. We have no information about the position of the line-laser probe. So, the 3D reconstruction is based solely on the displacements of the laser line in images taken by the cameras in our multi-camera-system. No target markers or background patterns are required, because the camera positions are known a priori. Thus, this approach is similar to the stereo-matching method we used in [4].

3 Prerequisites

A triangulation laser scanner usually consists of at least one camera and a line-laser probe. We use the multi-camera system with four color cameras, see Figure 1 (left), we built in a previous project [4, 9]. This camera system was designed for stereo-matching and 3D face reconstruction and recognition. The cameras are mounted in a planar upside down Y-constellation, see Figure 1 (middle). Thus, each pair of cameras has a different disparity direction to avoid potential problems with features aligned with a single disparity direction. The four cameras are synchronized such that the cameras take the images at the same time.

To extend this camera system to a laser scanner, two line-laser probes are used, see Figure 1 (right). Each of these probes consists of a laser emitter and a cylindrical lens. The lens spreads the laser beam to a fan such that a laser line is projected. An additional lens is used to focus the fan to a certain distance. This results in a sharper projection of the laser line. The two probes differ by the color of the laser and the light intensity: The red probe emits a 15mW laser line, the green probe emits a 5mW laser line. Using multiple laser colors allows to adapt to different material properties of scanned objects. The different light intensities are partially compensated by the sensor of the color cameras, which has twice as

Figure 1 A system of four Point Grey Flea®2 FireWire 800 cameras (left) arranged in an upside down Y-constellation (middle). Red and green line-laser probe (right).

much green as red pixels.

Unlike usual triangulation laser scanners, in our system the position of the line-laser probe is unknown. The operator holds one of the line-laser probes in his hand and points it towards the scanned object. For each camera, the visible 2D laser line is extracted, see Section 5. A specialized stereo-matching algorithm is used to reconstruct the 3D coordinates of all points on this line, see Section 6.

4 Calibration

Since we use a hand-held laser probe, there is no calibration of the laser probes required. So, for the calibration of the scanning system the following parameters are required:

1.1 Camera parameters:

- **a.** Aperture angle α of the cameras.
- **b.** Image height h and width w in pixels of the cameras given by their resolution.

1.2 Relative positions of the cameras.

The aperture angle is computed from the physical width of the area on a planar wall that is visible in the camera image at a one meter distance of the camera to the wall.

The cameras are mounted on a Y-shaped frame of angle plates, see Figure 1 (left) and (middle). Thus, there is one central camera, which will be used as reference for the other three so-called outer cameras. In an ideal camera system the cameras are perfectly co-planar, have parallel view directions, and the central camera has the same distance $\hat{t}$ to all three outer cameras in physical space. The outer cameras are mounted in (normalized) direction $\hat{t}_i \in \mathbb{R}^2, i = 1, 2, 3$, from the central camera, where the angles of $\hat{t}_i$ to the horizontal image direction are 90°, 210°, 330°. In image space the cameras have the relative positions $t_i = t \cdot \hat{t}_i$, where t is the distance measured in pixels of the image centers of the cameras. This can be computed as $t = \hat{t}/s$, where $s = 2\tan(\alpha/2) \cdot z/w$ is the size of one pixel in physical space, if the cameras are placed at a known distance z from a planar wall. This yields the theoretical relative camera positions t_i in image space.

Because of imprecisions in the construction of the Y-frame, the t_i have to be corrected. There is a translational error, because in practice the outer cameras do not have the same distance to the central camera. Due to the construction of the Y-frame, we assume that the relative rotational errors of the cameras around the view direction and the horizontal image

direction are negligible and the relative rotational errors around the vertical image direction are relatively small. Therefore, we assume that the latter can be estimated sufficiently accurate by an additional translational error.

To estimate the translational errors, the true distances in image space of a calibration object captured by all four cameras at the same time are computed. We use as calibration object a simple red laser-point projected onto a planar wall at distance z to the cameras. This laser-point gives a point p_i, $i = 1, 2, 3, 4$, in each camera's image. In an ideal camera system, p_i, $i = 1, 2, 3$, should appear in the image of the i-th outer camera at position $p_4 + t_i$, if p_4 is the point in the central camera. Thus, the translational error is

$$c_i = p_4 + t_i - p_i, \qquad \text{for } i = 1, 2, 3.$$

To measure p_i for each image, the center of the laser-point is detected as the maximum color value after applying a Gaussian blur filter to the image.

5 Line Extraction

For triangulation scanners based on stereo-matching of camera images, the depth of a 3D point can only be computed if it is visible by at least two cameras, see Section 6. Then, stereo-matching is the process of finding corresponding points in the camera images of two different cameras at different perspectives. To accelerate this process we only use points that are on laser lines. So, these laser lines have to be extracted from the images.

For precise depth estimations, the extracted lines must be one pixel wide and the points on the extracted lines need to be at sub-pixel accuracy. Furthermore, the extraction process must be robust to noise and must execute in real time. To satisfy these requirements, we adopt techniques from [2] and [5] in Steps **2.2.** and **2.3.** of our line extraction algorithm below.

Our line extraction algorithm is applied to every image and consists of five steps described below. It takes as input an image, which is given by $I : \{-w/2, \dots, w/2\} \times \{-h/2, \dots, h/2\} \to \mathbb{R}^3$, $(x, y) \mapsto (r, g, b)$, where (x, y) are pixel coordinates. The three coordinate functions I_r, I_g, and I_b of I represent the three color channels of the image.

Line Extraction Algorithm

2.1 Binarize the source image's red channel I_r (analogously for the green channel)

$$B_I(x, y) = \begin{cases} 1, & \text{if } I_r(x, y) > t_I \\ 0, & \text{otherwise.} \end{cases}$$

The threshold t_I is set manually. We use $t_I = 0.165$.
This step removes most of the information from the image that is not necessary for the line extraction. In B_I the laser lines are several pixels wide.

2.2 Convolve the binary image B_I with the phase coded disc O_{PCD}

$$Q(x, y) = \frac{1}{\pi r^2} \sum_{u=-r}^{r} \sum_{v=-r}^{r} B_I(x + u, y + v) \cdot O_{\text{PCD}}(u, v) \in \mathbb{C}, \tag{1}$$

where O_{PCD} is defined in (2) and the radius r of the disc is chosen to be larger than the maximum width of the laser line. Details are discussed in Section 5.1.
This step yields an image with maximal values at the line centers. This line of maxima is exactly one pixel wide.

2.3 A sub-pixel accurate non-maximum suppression NMS is applied to $|Q(x,y)|$ along direction $\mathrm{Arg}(Q(x,y))/2$ to mask the line of maxima from the rest of the image

$$N(x,y) = \mathrm{NMS}\left(|Q(x,y)|, \frac{1}{2}\mathrm{Arg}(Q(x,y))\right) \in \mathbb{R},$$

where $\mathrm{Arg}(z)$ is the principal value of the phase of a complex number z. Details are given in Section 5.2.

2.4 Binarize $N(x,y)$

$$B_N(x,y) = \begin{cases} 1, & \text{if } N(x,y) > t_N \\ 0, & \text{otherwise.} \end{cases}$$

The threshold t_N is set manually. We use $t_N = 0.15$.
This step yields a binary image with sequences of line center points, that are one pixel wide, and have well defined start and end points.

2.5 Subsume the center points in B_N to line segments. Line segments that are shorter than 50 points are ignored. Details are given in Section 5.3.

This line extraction algorithm is implemented in C++ and OpenGL Shading Language GLSL. The GPU is used for

- binarization of the images (Steps **2.1.** and **2.4.**),
- convolution with the phase coded disc (Step **2.2.**), and
- non-maxima suppression (Step **2.3.**).

Only the line tracing in Step **2.5.** is computed on the CPU.

5.1 Phase Coded Disc

In Step **2.2.** we use a convolution with a phase coded disc as in [2], which is defined as

$$O_{\mathrm{PCD}}(u,v) = \begin{cases} \exp(2i\,\mathrm{Arg}(u+iv)) & \text{, if } \sqrt{u^2+v^2} \le r, \\ 0 & \text{, if } \sqrt{u^2+v^2} > r, \end{cases} \tag{2}$$

where $\exp(2i\,\mathrm{Arg}(u+iv))$ is the exponential representation of a complex number whose phase is twice the phase of $u+iv \sim (u,v)$. Note that $\mathrm{Arg}(u+iv)$ is computed by $\mathrm{atan2}(v,u)$, the four-quadrant arctangent function.

Due to the doubling of the phase in (2), the phase angles rotate twice through $[0, 2\pi]$ as (u,v) rotates once around the origin on the phase coded disc O_{PCD}, see Figure 2. This has the effect that points, whose phase differs by 90°, have opposite phases (180° difference) on O_{PCD}. Thus, they attenuate in the convolution (1). On the other hand, points with the same or opposite phases have the same phase on O_{PCD}. Thus, they amplify in the convolution (1).

For the convolution of O_{PCD} with the binarized image B_I this has the effect, that the magnitude $|Q(x,y)|$ is relatively large, if at (x,y) the laser line contains the center of O_{PCD}, see Figure 2 (left). Otherwise, $|Q(x,y)|$ is relatively small, see Figure 2 (right). So, after convolving B_I with O_{PCD}, the maxima of $|Q|$ are located on the center of the laser line. However, lines with 90° corners cannot be detected with this approach.

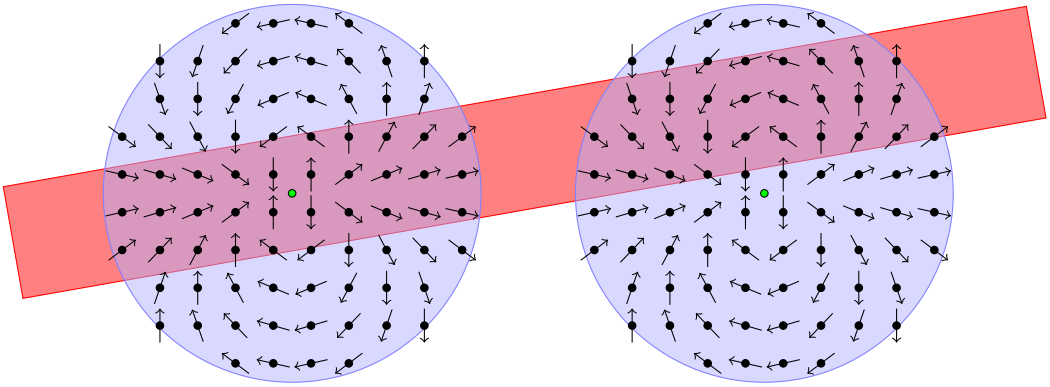

Figure 2 Phase coded discs with red laser line and small arrows visualizing the complex phase angles.

5.2 Non-maxima Suppression

To find sub-pixel accurate maxima in the convolution images, we adapted the approach of [5] in two ways. First, the magnitude of Q is used instead of the gradient's magnitude. Second, the normal $L^\perp$ to the laser line direction L is used instead of the gradient direction. The direction of the laser line $L(x, y)$ is determined by half the phase angle of $Q(x, y)$

$$L(x, y) = \frac{1}{2}\mathrm{Arg}(Q(x, y)).$$

Thus, $L^\perp(x, y)$ is perpendicular to L at (x, y).

Non-maxima Suppression

3.1 Denote by B the intersection of the line through A in direction $L^\perp$ with the line segment through the pixels A_i and A_{i+1} for a $i \in \{1, \ldots, 4\}$, see Figure 3. Analogously, C is the intersection in the opposite direction of A. Thus, the values of $|Q|$ at B and C are linearly interpolated between the values at A_i and A_{i+1} respectively A_{i+4} and A_{i+5}.

3.2 If there is no maximum at A compared to B and C, A is ignored in the result.

3.3 If there is a maximum at A, the sub-pixel accurate position is computed as the position along line $L^\perp$ of the maximum of the quadratic interpolant of the values at A, B, and C, see Figure 4.

Thus, we store per pixel the decimal places of the sub-pixel coordinates of the maximal value and the maximal value of $|Q|$.

5.3 Line Tracing

The extracted line center points in B_N have to be assigned to line segments. Thus, the output of Step **2.5.** is a list of line segments $(s_k)_k$ for each image. Each line segment s_k is a list of line center points $(p_{k,l})_{j=0}^{n_k}$.

Line Tracing

4.1 Identify start points $p_{i,0}$ in B_N by matching with the 3×3 pixel patterns in Figure 5 and generate a new segment s_k containing the start point $s_k = (p_{k,0})_l$. Start points, which are already part of a line segment, are ignored.

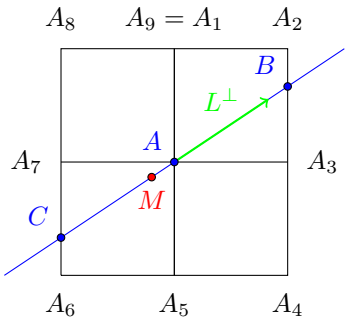

Figure 3 Sub-pixel accurate position of the maximum M on line segment CB [5].

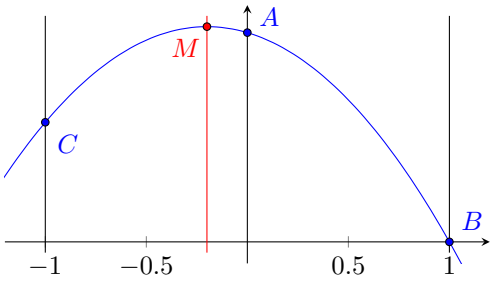

Figure 4 The quadratic interpolation of the values at A, B, C. At M is the maximum of the interpolant.

4.2 For a segment $s_k = (p_{k,0}, \ldots, p_{k,l})$ check the 8-neighborhood of point $p_{k,l}$ in B_N for pixels with value 1. If direct and diagonal neighbors are found, the former are preferred. If a new point $p_{k,l+1}$ is found, it is appended to the corresponding line segment $s_k = (p_{k,0}, \ldots, p_{k,l+1})$. Visited points are tagged to avoid multiple visits in Steps **4.1** and **4.2**.

4.3 Repeat step **4.2** until a point is identified as end-point matching the 3×3 pixel patterns in Figure 5.

4.4 An extracted line segment s_k is ignored, if it contains less than 50 points.

6 Depth Estimation

Similar to the stereo-matching method in [4], the spatial depth of the point data is reconstructed from the disparities between images. This requires a calibrated camera system

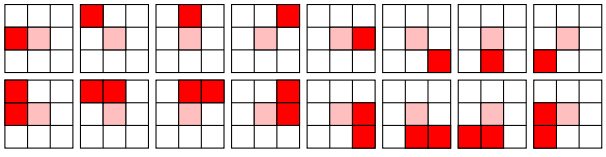

Figure 5 Start point patterns of 3×3 pixels: The white pixels have value 0 in B_N, the other pixels have value 1. Thus, the reddish pixels belong to a laser line. The pink pixel is the query pixel.

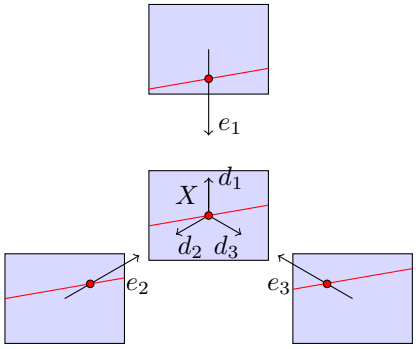

Figure 6 Schematic illustration of the four camera images with projections of epipolar lines e_i of a point X (red point) in the central camera's image on a laser line (red line), see [4].

whose lenses are corrected. For the lens correction we use the method [6, 4] to correct all camera images to a central projection in a pre-processing step. Then, the calibration as described in Section 4 is applied.

For our camera system at every instant of time a quadruple of images is generated containing one image I^i, $i = 1, 2, 3, 4$ of each camera. Accordingly, the above line extraction algorithm yields a quadruple of e.g. B_N^i where the super-script indicates the i-th outer camera for $i = 1, 2, 3$ or the central camera for $i = 4$. From the line extraction step (Section 5) we have three representations of the laser line per camera image: the line segments s_k^i, the binary image $B_N^i(x, y)$, and the sub-pixel accurate laser line center point in $N^i(x, y)$. For each point $p_{k,l}^4$ of the line segment s_k^4 of the central camera image, a depth is estimated using the images of the outer cameras:

5.1 Corresponding points in two camera images from two different cameras are identified along epipolar lines, see Section 6.1.

5.2 For each pair of corresponding points the depth is estimated by an inverse projection, see Section 6.2.

6.1 Epipolar Lines

After the calibration we assume that all four cameras of the camera system are co-planar and have parallel view directions. Therefore, a point $\hat{X}$ at infinite depth in physical space will have the same image coordinates X_i, $i = 1, 2, 3, 4$, in all four camera images I^i. A point $\hat{Y}$ not at infinity with image coordinates $Y_4 = X_4$ has image coordinates $Y_i \neq Y_4$, $i = 1, 2, 3$, in the outer cameras. As $\hat{Y}$ moves closer, Y_i, $i = 1, 2, 3$, moves along the negative camera direction $-d_i$. Thus, $\hat{Y}$ traces out a ray in physical space pointing away from the central camera. This line is called the *epipolar line* of X_4. The central projection of an epipolar line in the outer camera images is a straight line, too. Figure 6 shows the projections $e_i(X)$ of an epipolar line of X for the camera system, schematically.

For every point $p_{k,l}^4$ the epipolar line is computed and projected to the outer camera images. The resulting epipolar line projections $e_i(p_{k,l}^4)$, $i = 1, 2, 3$, are rendered to image I^i using the Bresenham algorithm [1]. If during this rendering a pixel is set that is also set in $B_N^i(x, y)$ an intersection of the epipolar line e_i with a line segment in I^i is detected. The pixel distance between $p_{k,l}^4$ and the sub-pixel accurate laser line position from $N^i(x, y)$ at the intersection is the so-called *disparity* $d_i(p_{k,l}^4)$. So, there are up to three disparities d_i, $i = 1, 2, 3$, for each $p_{k,l}^4$.

To improve the quality of the reconstruction, we use subsequently the average $d(p^4_{k,l})$ of the two disparities that are closest to each other. If there are less than two disparities or the two closest disparities differ too much, the computations for $p^4_{k,l}$ are aborted.

6.2 Inverse Projection

With the average disparity d, the depth c_z in physical space of $p^4_{k,l}$ is estimated by

$$c_z = \frac{w\hat{t}}{2\tan\left(\frac{\alpha}{2}\right)d},$$

where α is the aperture angle of the camera, w the image width in pixels, and $\hat{t}$ the camera distance in physical space. The depth c_z together with the pixel coordinates $p^4_{k,l}$ allow an inverse projection of $p^4_{k,l}$ to 3d coordinates $[c_x, c_y, c_z]^T$ in physical space as

$$\begin{bmatrix} c_x \\ c_y \end{bmatrix} = 2\,\frac{c_z \cdot p^4_{k,l}}{w}\tan\left(\frac{\alpha}{2}\right) = p^4_{k,l}\frac{\hat{t}}{d}.$$

7 Results

To demonstrate the effectiveness of our laser scanner system, we scanned a test scene of three wooden bricks shown in Figure 7(a). The exposure of the cameras was reduced to achieve a better contrast between the laser line and the surroundings, see Figure 7(b). During a period of five minutes, we captured ca. 210,000 points at a rate of two image-quadruples per second.

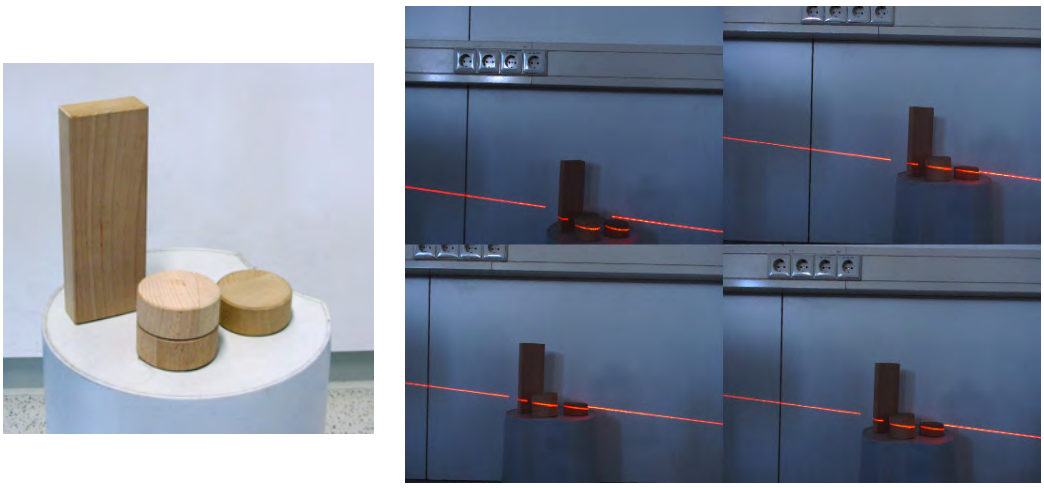

(a) (b)

Figure 7 Test scene consisting of four wooden bricks (a) and the four images of the test scene scanned with a red laser line captured by the camera system (b).

Figure 8 shows a front and a top view of the computed point cloud. The overall quality of the data allows to recognize the shapes of the different wooden bricks, especially the one in the foreground. The reconstruction has a higher quality and is more robust than the pure stereo-matching method in [4]. However, an elaborate comparison with other triangulation methods is doomed by the high costs for other hand-held triangulation devices.

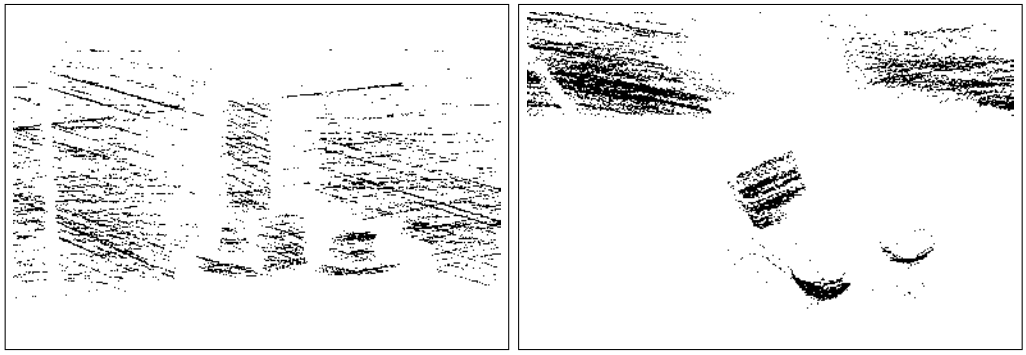

Figure 8 Point cloud from two different perspectives (left: front view, right: top view) of the test scene in Figure 7 scanned with a red laser line.

The scan lines in the point clouds show some small periodic noise in view direction of the cameras. We think this might be caused by three effects:

- Aliasing at the line extraction Step **2.2.**: The binarization $B_I(x, y)$ in Step **2.1.** creates an aliased image of the laser line. In particular, if the aliasing occurs on both sides of the line simultaneously, this may cause small steps in the detected line centers.
- Intersection of e_i with the line segments in I^i in Section 6.1: The laser line position from $N^i(x, y)$ is at sub-pixel accuracy while the projected epipolar line e_i is not. Although this approximation does not affect the disparity d_i very much, a more precise intersection of the line segment with e_i could improve the results.
- Calibration in Section 4: The laser point is not detected at sub-pixel accuracy.

Another effect that we observe in the scan data is that some of the scanned laser lines appear more than once in the data at slightly different depths. This is caused by blurry camera images, e.g. by motion blur. Additional filtering after the detection of the line centers (Section 5, Step **2.2.**) could be used to avoid these artefacts.

8 Conclusion and Outlook

We demonstrated in this paper how to build a laser scanner device at low costs using an existing camera system. The presented reconstruction algorithm runs on the GPU and is fast enough to compute 3D point data during the scan. Despite the remaining problems (see Section 7) the reconstruction yields better quality and is more robust than the pure stereo-matching method in [4].

Our laser scanner is limited to scanning from a single camera position. This only allows to capture one side of an object. For complete scans of objects it is necessary to either move the camera system or rotate the object e.g. on a turn table. Combining such scans from different directions usually requires an *iterative closest point* algorithm.

It is possible to improve the quality of the scanned results in a post-processing step. All points on a laser line lie in the plane of the laser line fan. Thus, fitting this plane to each scan line and projecting the points onto this plane along the view direction of the cameras will probably solve most problems described in Section 7 and will be implemented soon.

Acknowledgments This work was supported by DFG UM 26/5-1 and DFG GK 1131.

References

1 J.E. Bresenham. Algorithm for computer control of a digital plotter. *IBM Systems Journal*, 4(1):25–30, 1965.

2 S. P. Clode, E. E. Zelniker, P. J. Kootsookos, and I. V. L. Clarkson. A phase-coded disk approach to thick curvilinear line detection. In *Proceedings of the 12th European Signal Processing Conference*, pages 1147–1150, 2004.

3 K. Denker, B. Lehner, and G. Umlauf. Real-time triangulation of point streams. *Engineering with Computers*, 27(1):67–80, 2011.

4 K. Denker and G. Umlauf. Accurate real-time multi-camera stereo-matching on the gpu for 3d reconstruction. *Journal of WSCG*, 19(1-3):9–16, 2011.

5 F. Devernay. A non-maxima suppression method for edge detection with sub-pixel accuracy. Technical Report RR-2724, INRIA, 1995.

6 F. Devernay and O. Faugeras. Straight lines have to be straight: automatic calibration and removal of distortion from scenes of structured enviroments. *Mach. Vision Appl.*, 13(1):14–24, 2001.

7 G. Frankowski, M. Chen, and T. Huth. Real-time 3d shape measurement with digital stripe projection by texas instruments micro mirror devices DMD™. *Three-Dimensional Image Capture and Applications III*, 3958(1):90–105, 2000.

8 Y. Furukawa and J. Ponce. Accurate, dense, and robust multi-view stereopsis. In *CVPR*, pages 1–8, 2007.

9 J. Hensler, K. Denker, M. Franz, and G. Umlauf. Hybrid face recognition based on real-time multi-camera stereo-matching. In G. Bebis et al., editors, *Advances in Visual Computing*, volume 6939 of *Lecture Notes in Computer Science*, pages 158–167, 2011.

10 R. A. Jarvis. A laser time-of-flight range scanner for robotic vision. *IEEE Trans. Pattern Anal. Mach. Intell.*, 5(5):505–512, 1983.

11 R. A. Jarvis. A perspective on range finding techniques for computer vision. *IEEE Transactions on Pattern Analysis and Machine Intelligence*, 5(2):122–139, 1983.

12 A. Klaus, M. Sormann, and K. Karner. Segment-based stereo matching using belief propagation and a self-adapting dissimilarity measure. In *Proc. of the 18th Int. Conf. on Pattern Recognition*, pages 15–18, 2006.

13 J. L. Posdamer and M. D. Altschuler. Surface measurement by space-encoded projected beam systems. *Computer Graphics and Image Processing*, 18(1):1 – 17, 1982.

14 D. Scharstein and R. Szeliski. A taxonomy and evaluation of dense two-frame stereo correspondence algorithms. *Int. J. Comput. Vision*, 47(1-3):7–42, 2002.

15 C. Teutsch. *Model-based Analysis and Evaluation of Point Sets from Optical 3D Laser Scanners*. Shaker Verlag, 2007.

16 A. Wehr and U. Lohr. Airborne laser scanning - an introduction and overview. *ISPRS Journal of Photogrammetry & Remote Sensing*, 54(2-3):68–82, 1999.

17 S. Winkelbach, S. Molkenstruck, and F. M. Wahl. Low-cost laser range scanner and fast surface registration approach. In *DAGM-Symposium*, pages 718–728, 2006.

18 R. Yang and M. Pollefeys. A versatile stereo implementation on commodity graphics hardware. *Real-Time Imaging*, 11(1):7–18, 2005.

19 S. Zhang and S.-T. Yau. High-resolution, real-time 3d absolute coordinate measurement based on a phase-shifting method. *Opt. Express*, 14(7):2644–2649, 2006.